



Automated segmentation of human brain MR images using a multi-agent approach

Nathalie Richard^{a,b}, Michel Dojat^{a,b,*}, Catherine Garbay^b

^aUnité Mixte INSERM/UJF U594, LRC CEA 30V, Centre Hospitalier Universitaire - Pavillon B, BP 217, 38043 Grenoble Cedex 9, France

^bLaboratoire TIMC-IMAG, Institut Bonniot, Faculté de Médecine, Domaine de la Merci, 38706 La Tronche Cedex, France

Received 3 April 2003; received in revised form 7 October 2003; accepted 29 November 2003

Abstract

Image interpretation consists in finding a correspondence between radiometric information and symbolic labeling with respect to specific spatial constraints. It is intrinsically a distributed process in terms of goals to be reached, zones in the image to be processed and methods to be applied. To cope with the difficulty inherent in this process, several information processing steps are required to gradually extract information from the gray levels in the image and to introduce symbolic information. In this paper we advocate the use of situated cooperative agents as a framework for managing such steps. Dedicated agent behaviors are dynamically adapted depending on their position in the image, of their topographic relationships and of the radiometric information available. The information collected by the agents is gathered, shared via qualitative maps, or used as soon as available by acquaintances. Incremental refinement of interpretation is obtained through a coarse to fine strategy. Our work is essentially focused on radiometry-based tissue interpretation where knowledge is introduced or extracted at several levels to estimate models for tissue-intensity distribution and to cope with noise, intensity non-uniformity and partial volume effect. Several experiments on phantom and real images were performed. A complete volume can be segmented in less than 5 min with about 0.84% accuracy of the segmented reference. Comparison with other techniques demonstrates the potential interest of our approach for magnetic resonance imaging (MRI) brain scan interpretation.

© 2004 Elsevier B.V. All rights reserved.

Keywords: Image processing; Medical imaging; Segmentation; Cooperation; Information fusion

* Corresponding author. Tel.: +33-4-76-76-57-48; fax: +33-4-76-76-58-96.

E-mail addresses: nrichard@ujf-grenoble.fr (N. Richard), michel.dojat@ujf-grenoble.fr, mdojat@ujf-grenoble.fr (M. Dojat), catherine.garbay@imag.fr (C. Garbay).

1. Introduction

Image interpretation consists in finding a correspondence between radiometric information (gray levels in the image) and symbolic labeling under specific spatial constraints. The interpretation of 3D magnetic resonance imaging (MRI) brain scans is oriented towards two different goals, namely identifying tissue or anatomical structures. Three tissue classes exist in the brain: gray matter (GM), white matter (WM) and cerebro-spinal fluid (CSF) distributed over several anatomical structures, such as cortical ribbon and central structures (GM), myelin sheath (WM), ventricles and sulci (CSF). To localize tissue and label voxels accordingly, radiometric knowledge (i.e. knowledge about the intensity distribution for each tissue class, as well as knowledge about the image acquisition artifacts), has to be inserted. In addition, anatomical knowledge (i.e. knowledge about the geometry and localization of the anatomical structures), must be inserted to drive the structure identification process. Tissue identification can be a prerequisite for structure identification. In turn, this latter process allows the introduction of new tissue classes for modeling the observed inter-structure variability of intensity distributions, thus contributing to the refinement of the intensity-based tissue interpretation process.

Interpreting MRI brain scans is a difficult task for several reasons: (1) the volume of data to be processed is huge (≈ 10 Mb for one 3D image); (2) the anatomy of cerebral structures is complex and highly variable between subjects; and (3) the radiometric characteristics of these structures show high variability and low specificity due to image acquisition artifacts.

Three kinds of acquisition artifacts are taken into account in general: (1) a white noise is observed over the whole image volume, which affects tissue-intensity range and leads to overlapping of tissue intensity distributions; (2) intensity non-uniformities are observed mainly due to imperfections of the MRI device (bias field); (3) a partial volume effect is observed due to the sampling grid of the MRI signal, which leads to tissue mixtures inside some voxels (whose gray levels then follow specific distributions, which are different to those of pure tissue).

Dedicated modeling and fusion mechanisms have to be interleaved and carefully controlled to face these difficulties, as shown in Fig. 1.

1.1. Modeling process (see the Y-axis in the Fig. 1)

To gradually construct the image interpretation, two knowledge levels are commonly used, which are more or less explicitly expressed depending on the approach:

- *The voxel level*, where information about each voxel is stored in spatially organized maps.
- *The model level*, where tissue class characteristics are described using different parameters and probability distributions. This information is given as a prior knowledge to the system or learned and refined during the interpretation process.

When no prior knowledge is provided, several mechanisms are required and interleaved to manage these two tightly connected levels. During the estimation step, model parameters are estimated from voxel radiometric characteristics and from previously computed interpretation maps. During the classification step, the model-based probability (distance to class model) that a voxel belongs to a tissue class is computed.

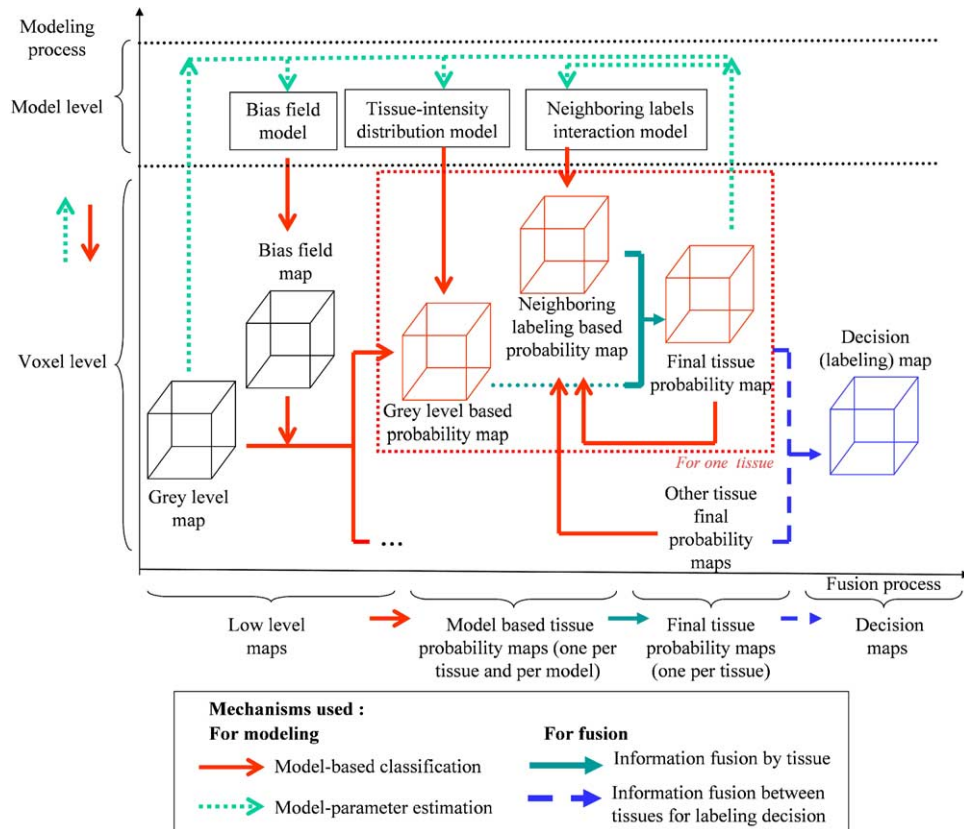


Fig. 1. The interpretation process as a combination of modeling and fusion processes. The interpretation process is distributed along two axes: the modeling axis (Y-axis), where interleaving between model and voxel information takes place, and the fusion axis (X-axis) where gradually acquired knowledge allows a progressive refinement of the interpretation. At the voxel level, acquired knowledge is gathered in various maps. At the model level, three models, for bias field, tissue-intensity distribution and neighboring interactions are considered. Note that the modeling and fusion processes rely on several mechanisms which are tightly interleaved: model estimation is continuously applied to refine the knowledge gained and then fused to obtain the final decision maps.

In the literature, several models have been proposed, to characterize tissue intensity distributions [2,16,24,29,32], to respect tissue homogeneity based on interactions between neighboring voxel labels [22,31] and to introduce corrections for intensity non-uniformity [1,2,21,25,28,30], or partial volume effect [12,17,23,25].

1.2. Fusion process (see the X-axis in the Fig. 1)

The model-based probabilities for each tissue are computed and aggregated using fusion mechanisms at the voxel level to obtain a final probability map for each tissue. Membership probabilities for the various tissues may then be confronted so that the final labeling

decision can be made for each voxel. To be combined, the information obtained must be modeled in a common framework that manages imprecision and uncertainty [4]. A Bayesian probabilistic framework is most often considered [31,33]. Uncertainty and imprecision modeling may also be introduced, using the fuzzy [1,14,21], or possibilistic [3], approaches.

1.3. Control strategy

Starting from gray level maps, the interpretation process leads to progressively more refined labeling decisions through several modeling and fusion steps. Model parameters should preferably be learned from the gray levels rather than given a priori to the system in order to strengthen its ability to adapt. When several models and maps are introduced to tackle with the artifact issues, an high number of parameters have to be estimated. Control strategy is thus a crucial issue. It drives spatial exploration of the image volume and evolution of the interpretation process as shown in the graph in Fig. 1. It decides (1) when a given model should be introduced, instantiated and used to interpret the image, and (2) how a given model should be spatially specified, i.e. from which image region it should be learned or which image region it should be used to interpret.

The complexities of brain scan segmentation lead us to advocate the use of a local estimation and classification strategy. Such a strategy allows the careful adaptation of the analysis to the specificities of the zone under interest (for instance in term of the anatomical structures whose presence may hamper the modeling process). Each decision or model is situated in a specific local context, incrementally enriched along the interpretation process. Any decision that is easy to take is immediately performed and the produced information is at once used to help further decision making. Any decision that is difficult to take (the validation of a model, the launching of labeling) is delayed. We propose the situated and cooperative agent paradigm to implement our decentralized local strategy and design an opportunistic data-driven interpretation system.

The structure of the paper is as follows: Section 2 is devoted to presentation of the proposed method and to details concerning the multi-agent architecture. Section 3 is devoted to the evaluation methodology. Results are presented in Section 4. In Section 5, we discuss several aspects of our work in the light of other approaches.

2. Material and method

We essentially focus our work on radiometry-based tissue interpretation where knowledge is introduced or extracted at several levels to instantiate models for class distribution and to tackle artifact problems.

2.1. Rationale

The interpretation process should be performed in a situated way i.e. *inside distributed regions of interest, under evolving goals*, and under control of *dedicated mechanisms* function of the state of the process.

2.1.1. Focalization on distributed regions of interest

To take into account the non-uniformity of intensity distribution over the image, primarily due to bias field and secondly to inter-structure variability of tissue intensity, we perform the interpretation locally on small volume partitions. Local radiometric models are introduced, which are computed during steps to estimate local tissue intensity distribution and used during local labeling steps. Because estimation is performed locally, the resulting models are prone to error and some are missing [12,16,22,34]. To cope with this difficulty, every local model is confronted with models interpolated from the neighborhood. In this way, we maintain the global consistency of the distributed interpretation process and reinforce the robustness of the models.

2.1.2. Evolving goals: a two-phase model estimation and voxel-labeling process

To take into account the noise and partial volume effect, which induce errors in model estimation and voxel labeling, two phases are distinguished in the interpretation process, based on the progressive relaxation of labeling constraints. Each phase consists of two steps: radiometric model estimation and voxel labeling.

During the *initial phase*, an under-segmentation of the image is produced, based on region-growing mechanisms and strict labeling constraints. Model parameters are firstly estimated from the local intensity distribution. Similarly to [12,25,23], we estimate models dedicated to the intensity distribution of voxels containing mixture of tissues. Model parameters are then used to define strict labeling constraints. Starting from robust seeds, the labeling of voxels is performed by sequentially evaluating the voxels situated at the boundary with the tissue region previously labeled (the so-called “candidate voxels”). To evaluate voxels two criteria are combined: a “radiometric criterion” (based on the voxel gray level) and a “topological criterion” (based on the current labeling of neighboring voxels). No labeling decision is taken at this point for the most difficult voxels essentially located at the tissue boundaries. These voxels have an atypical gray level value mainly due to partial volume effect.

During the *final phase*, the radiometric models are re-estimated using the previously obtained under-segmentation. The difficult to label voxels are then evaluated using these refined radiometric models together with a new labeling mechanism (so-called “competitive labeling”), which is more sophisticated and computationally intensive. At the beginning of the final phase, specific labels corresponding to voxels containing a tissue mixture may also be introduced by the user.

2.1.3. Decentralized control and coordination mechanisms for an information-driven interpretation process

Control is decentralized: the switch between local interpretation steps is performed autonomously in each volume partition as soon as the required information has been locally produced or provided from neighboring volume partitions. Distributed processes have to be coordinated inside a given volume partition and between neighboring partitions, function of the incrementally extracted knowledge available.

To launch the labeling steps, local models have firstly to be computed in the volume partition and a sufficiently robust model interpolation from the neighborhood has to be available to check the consistency of a given local model. For the purposes of coordination,

each time a model is modified, the corresponding information is propagated to neighboring regions. The labeling process performed during the initial phase requires information about the location of seeds to launch the region growing mechanism. A time-consuming process may be used to select seeds. This can be advantageously replaced by a partition-to-partition propagation, especially when rooting is difficult because few points belonging to a tissue can be present in a volume partition. To cope with such cases and accelerate labeling, when a given region growing process reaches the boundary of a partition, it transmits the list of candidate voxels to the corresponding neighboring processes, which may or may not already have been launched, depending on whether a robust seed has already been selected or not. The final estimation step is launched as soon as a sufficiently large local under-segmentation is available or when no more voxels can be locally labeled.

Distributed control and coordination mechanisms provide an opportunist system where information is extracted incrementally, the most robust one being extracted first and used to help further decision-making. Coordination is mainly an *information-driven process*: local processes are launched reactively as soon as sufficient robust information is available.

2.2. Our situated and cooperative agent-based approach

We introduce situated and cooperative agents as a programming paradigm to implement the previously described mechanisms. Situated and cooperative agents borrow from reactive AI the principle of *autonomy*, each agent acquiring the knowledge necessary to reach its own goal autonomously. From situated cognition [7], they borrow the principle of *contextual localization*, each agent being situated in a local evolutive context with specific neighborhood constraints to preserve the global consistency of the interpretation process. From multi-agent theory, they borrow the principle of *cooperation*, each agent interacting with its acquaintances to reach its goal. The system is composed of agents driven by a system manager, whose role is to manage their creation, destruction, activation and deactivation. Each agent is in turn provided with several behaviors whose selection is driven by a behavior manager. The launching of a given agent or behavior is context-dependent, driven by a simple synchronization model. The agents are organized in groups [13] driven by a group manager which ensures coordination (see Fig. 2).

2.2.1. Agent definition

Three types of agents coexist in the system (Fig. 3): global and local control agents and tissue-dedicated agents.

The role of the global control agent is to perform specific tasks dedicated to the whole image and to create local control agents distributed over the volume of the image. Distribution follows a regular 3D grid, where nodes are spaced at a distance D_l .

The role of local control agents is to create tissue-dedicated agents, to estimate model parameters and to confront tissue models for final labeling decisions. Two territories, centered at a given node on the partition grid, are assigned to each local control agent: a “perception territory”, a cube with a length equal to D_p in which model estimation activity will take place; and a “labeling territory”, a cube with a length equal to D_l ($D_p \geq D_l$), in which classification activity will take place. The perception territories of neighboring local control agents may overlap to reinforce coherence between adjacent models.

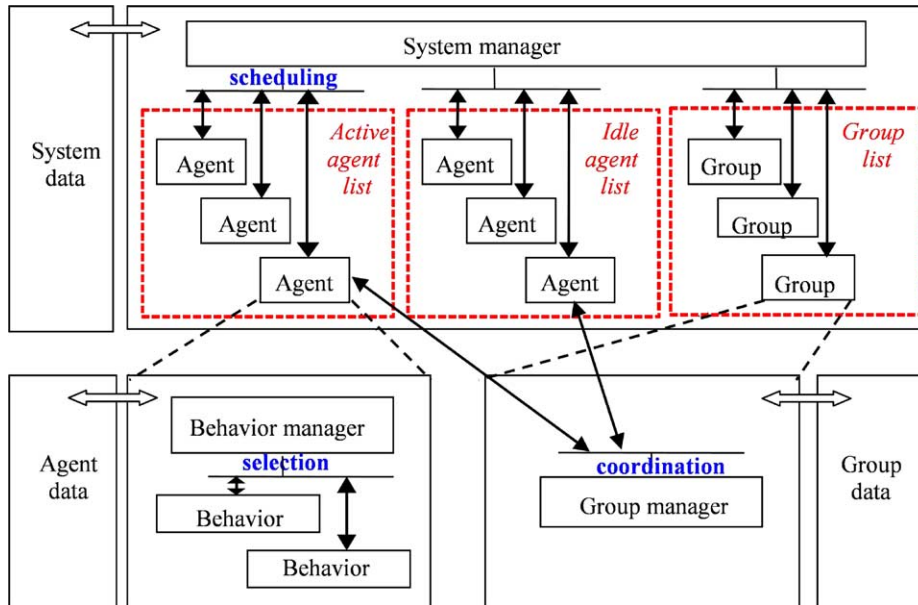


Fig. 2. The Multi-agent framework: the parallel execution of agents is simulated. The system manager launches agent execution in a sequential way. It can deactivate (respectively activate) and active (respectively idle) agents. Each agent is in turn provided with several behaviors whose selection is driven by a behavior manager. Behavior execution may consist in the iterative execution of an elementary task such as evaluating and labeling a voxel (region-growing behavior) or evaluating and selecting a seed voxel (rooting behavior). Agents are organized into groups driven by a group manager which ensures their coordination. Black arrows indicate the links between the different components.

The role of tissue-dedicated agents is to execute tasks distributed by tissue type, namely interpolation of tissue models from the neighborhood and the labeling of voxels using a region-growing process.

This type of design allows processing tasks to be distributed according to three different contexts:

- the whole image volume for the global control agent;
- a given zone in the image volume for local control agents;
- a given zone and tissue type for tissue-dedicated agents.

Progress along these successively more precise contexts allows gradually refined control and adaptation of the interpretation process.

2.2.2. Agent behaviors

Fig. 4 gives an overview of system distribution and sequencing. As already mentioned, the interpretation process consists of two phases, each composed of a model estimation and a classification step.

The control task is carried out as a control agent behavior as detailed below and detailed in further sections:

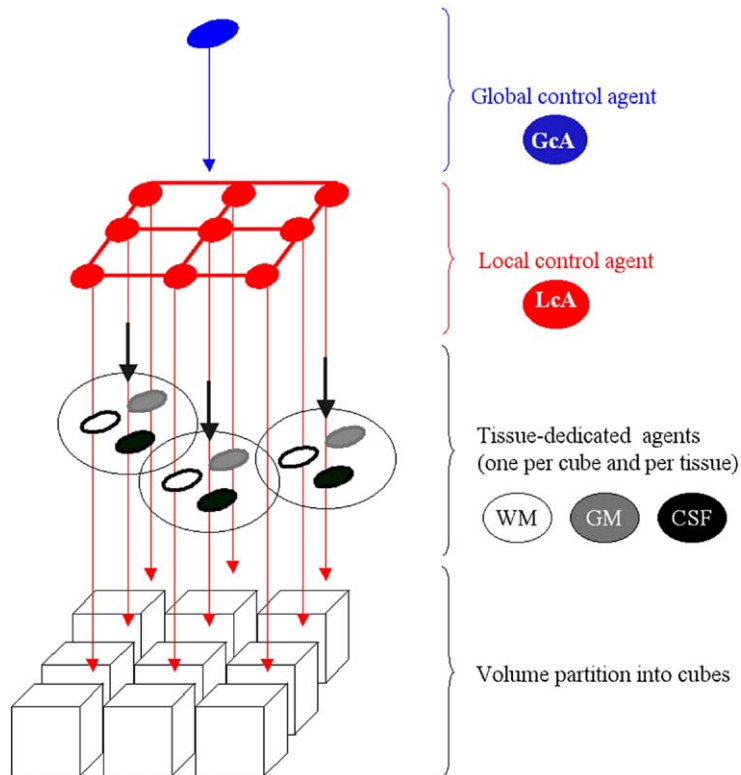


Fig. 3. Three types of agents co-exist in the system: global and local control agents, whose role is to build the processing model of the system, and tissue-dedicated agents, whose role is to execute tissue-centered analysis tasks.

- LcA1: *Initial radiometric modeling*—the local radiometric models are computed and, when available, given to the tissue-dedicated agents (see Section 2.2.4).
- LcA2: *Computation of region growing thresholds*—the thresholds used to control the region-growing process are dynamically computed from the local models (see Section 2.2.5).
- LcA3: *Final radiometric modeling*—the initial models are refined, based on labeling previously performed by tissue-dedicated agents (see Section 2.2.4).
- LcA4: *Competitive labeling*—unlabeled voxels are classified using a competitive evaluation function (see Section 2.2.5).

Similarly, tissue-dedicated tasks are implemented as agent behaviors:

- TdA1: *Radiometric model checking*—the locally estimated tissue-intensity model is compared to neighboring models of the same tissue (see Section 2.2.4).
- TdA2: *Rooting*—a position to start the region-growing process is iteratively searched (see Section 2.2.5).
- TdA3: *Region growing*—an iterative evaluation of voxels located at tissue boundary is performed (see Section 2.2.5).

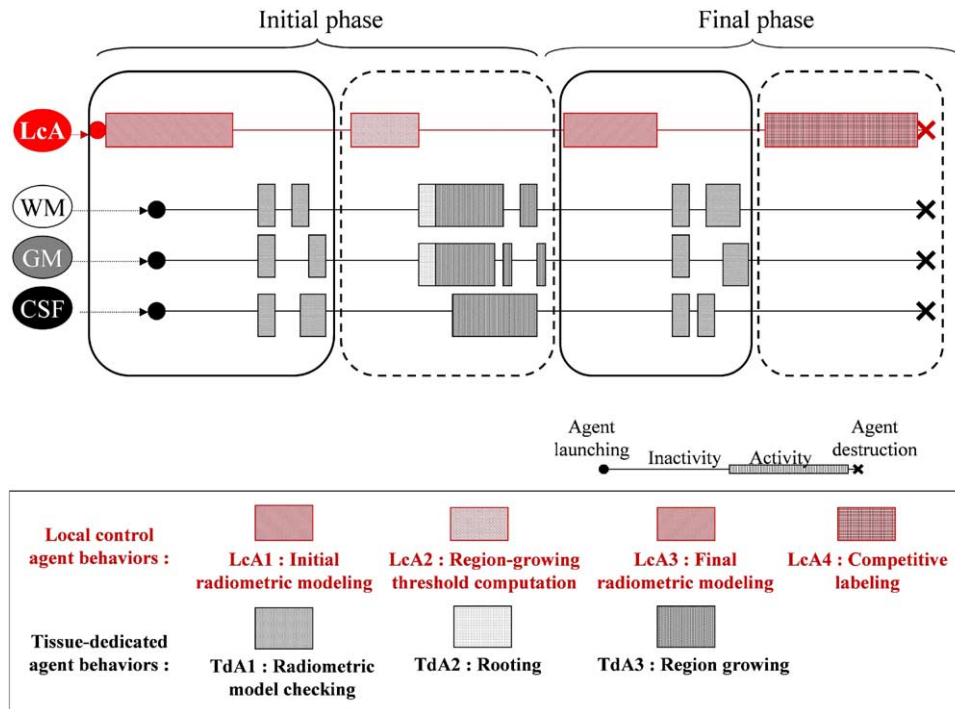


Fig. 4. Overview of task execution. Black and dashed lines, respectively, indicate model estimation and voxel classification. The sequencing of tasks is described horizontally. For each local control agent (LcA), several behaviors are successively executed during the initial and the final phases, respectively. These behaviors are: initial radiometric modeling, computation of region-growing thresholds, final radiometric modeling and competitive labeling. Tissue-dedicated agents (i.e. WM, GM and CSF agents in the figure), perform radiometric model checking, rooting and region-growing behaviors under the control of local agents. Note that during the final phase, these agents execute only one behavior, namely radiometric model checking, following the introduction of refined models by local control agents (LcA3). Labeling is then performed by the local control agents.

2.2.3. Information management and agent coordination

The agents share a common information zone, organized according to tissue type and spatial relations, which stores global and local statistical information. Qualitative information maps are introduced to efficiently gather, retrieve and easily add complementary information, such as the number of neighboring voxels with a given label.

The agents interact implicitly via information sharing and explicitly via behavior triggering and activation–deactivation process. When an agent produces robust information, it stores it in the common sharing zone, adapts its activity and triggers its acquaintances, i.e. the list of agents dedicated to the neighboring regions. Then, acquaintances dedicated to the same tissue interact during their model checking behavior (see Section 2.2.4) in both initial and final phases and during their rooting/region growing behaviors (see Section 2.2.5). Similarly, each agent owns a list of agents devoted to the same partition of the image (local control or tissue dedicated agents). This allows the

behavior switching between model estimation (*LcA1* and *LcA4*) to model checking (*TdA1*). This is also the means for tissue-dedicated agents to detect that their own models have been validated at the end of the model checking behavior (*TdA1*) and to launch the next local control agent behavior (*LcA2* in the initial phase and *LcA4* in the final phase).

When the agents cannot validate themselves the information produced during their local behavior, the switch to the next step of the interpretation process is delayed until all the remaining agents, from which depend the decision making, have obtained sufficiently reliable information. For this purpose, agents are organized into groups depending on their type and the processing step they are currently performing. Four local control agents groups (corresponding to the estimation and labeling tasks for each phase) and three tissue dedicated agents groups (corresponding to the estimation task for the both phases and to the labeling task for the initial phase) coexist in the system (see Fig. 4). When an agent switches its behavior, it leaves its group and enters in a new one corresponding to its new behavior. Such mechanisms are used to validate models interpolated from the neighborhood (see Section 2.2.4) and to obtain the largest possible under-segmentation when the labeling ratio can not be reached (see Section 2.2.5).

2.2.4. Local statistical models for radiometric modeling

Similarly to other approaches, distributions of gray levels are modeled as Gaussian curves for both pure tissue [24,32], and mixed tissue classes [23]. The mean values and standard deviations of these Gaussian curves, (μ_t, σ_t) with $t \in \{\text{CSF, GM, WM, CSF/GM, GM/WM}\}$, have to be estimated. For this purpose, estimation–maximization (EM) algorithms are applied locally during both initial and final phase by the local control agents. The EM algorithm is applied in the context of Bayesian classification with estimation of maximum likelihood of the Gaussian parameters. The prior probability is uniform and based on the relative frequency of each class in the volume. It is estimated for each iteration of the algorithm. In order to improve performance of the algorithm, we compute the local histograms on the agent perception territories and then estimate the model parameters using EM algorithm. During the estimation step of each iteration of the algorithm, the posterior probability for every possible gray level value (with non-zero frequency in the histogram) of belonging to a tissue class is calculated, instead of computing it from the gray level of each voxel. During the maximization steps, the Gaussian parameters (mean, standard deviation and weight) are computed using these previously obtained posterior probabilities and the frequency of each gray level obtained from the histograms.

2.2.4.1. Initial phase. This corresponds to the behavior *LcA1*. A set of five Gaussian curves is considered, whose parameters are estimated by the local control agents from the gray levels of the whole perception territory. EM algorithm is known to be highly sensitive to initialization. As a consequence, Gaussian parameters reasonably close to the researched models must be provided for initialization. To compute these parameters, the global image volume is initially clustered into three pure tissue classes using the fuzzy-C means algorithm. The membership degree for each gray level to each pure tissue is then used to compute the mean value and standard deviation of gray levels inside each partition. Partial volume class parameters are then supposed to be equal to the mean value of the two

pure tissue class parameters of which they composed. When any unrealistic model is computed, it is detected, based on the knowledge of the pure tissue Gaussian curve and then eliminated.

2.2.4.2. Final phase. This corresponds to the behavior *LcA3*. The initial phase supplies an under-segmented image where most of the voxels containing tissue mixtures, generally situated at the boundary of the tissue, remain unlabeled. To label these points, refined radiometric models are computed for each pure tissue type using the EM algorithm, based on previously labeled voxels in the perception territory.

2.2.4.3. Radiometric model checking. The consistency of the locally estimated models is checked at the end of the estimation step for each phase, by confrontation with a reference model computed from neighboring local models. This corresponds to the *TdA1* behavior. At each execution of this behavior, a reference model is interpolated from the neighborhood by computing the mean value of the neighboring models weighted by the inverse distance between each neighbor and the neighborhood center. If the distance between the estimated model and the reference model is too large (superior to fixed thresholds for each parameter μ_t and σ_t) or if no local model is available, the reference model is taken to replace the estimated or missing one. As long as this behavior is selected, its execution is triggered each time a local model is modified in the neighborhood. Any agent can autonomously select a model and stop the execution of the behavior when it considers its model as reliable enough, i.e. as soon as the locally estimated model is close to the reference model. The local control agent starts then the labeling step when valid models for all tissues in the perception territory have been selected. When the valid model is provided from the reference model, the behavior change of the agent is triggered by a group coordination mechanism, when all models are close enough to their neighboring models (i.e. when all tissue-dedicated agents remaining inside the group dedicated to this step of the interpretation process become inactive).

2.2.5. Voxel labeling

2.2.5.1. Initial phase. Strict region-growing constraints are defined in this first phase from the Gaussian models in order to label only the most reliable voxels of each pure tissue. This type of approach leads to an under-segmentation of the image.

Threshold computation. This is performed by the *LcA2* behavior, which is triggered when the tissue models of all the tissue-dedicated agents in the considered partition have been checked. For each pure tissue class, two radiometric criteria, computed from the corresponding radiometric model, are used to eventually aggregate a voxel v with intensity $I(v)$ to a tissue region t :

- a necessary radiometric criterion:

$$I(v) \in \{\eta_1^t, \eta_2^t\} \quad (1)$$

- a sufficient radiometric criterion:

$$I(v) \in \{\gamma_1^t, \gamma_2^t\} \quad (2)$$

where $\gamma_1^t \leq \eta_1^t$ et $\gamma_2^t \geq \eta_2^t$

These intervals are not fixed a priori. They are computed as follows:

$$\eta_1^t|_{\text{model}} = \mu_t - \sigma_t \times \alpha_S, \quad \eta_2^t|_{\text{model}} = \mu_t + \sigma_t \times \alpha_S,$$

and

$$\gamma_1^t|_{\text{model}} = \mu_t - \sigma_t \times \alpha_N, \quad \gamma_2^t|_{\text{model}} = \mu_t + \sigma_t \times \alpha_N$$

Parameters α_S and α_N are defined by the user (typical values are $\alpha_S = 1.5$ and $\alpha_N = 2$). Intervals from different tissues are then mutually adjusted to avoid superposition. For instance the sufficient criteria of GM is computed as follows:

$$\eta_1^{\text{GM}} = \max(\eta_1^{\text{GM}}|_{\text{model}}, \eta_2^{\text{CSF}}|_{\text{model}}) \quad \text{and} \quad \eta_2^{\text{GM}} = \min(\eta_2^{\text{GM}}|_{\text{model}}, \eta_1^{\text{WM}}|_{\text{model}})$$

Voxels whose intensity respects the sufficient criterion are aggregated to the tissue region. Voxels whose intensity does not respect the necessary criterion are rejected and are not aggregated to a region during the initial phase.

For voxels whose intensity respects only the necessary criterion, a third *topological criterion*, relative to the number of neighbors already aggregated to the region, is taken into account.

It is based on the compactness ratio $L(v, t)$ computed as the amount of neighbors of voxel v labeled with label t divided by the total amount of neighbors (in general 18). A threshold R_t , set by the user (typically $R_t = 0.75$) is introduced:

- a *topological criterion*:

$$L(v, t) > R_t \tag{3}$$

Rooting. Region-growing seeds are selected either under a robust criterion (so-called “rooting mechanism”) or transmitted from neighboring regions (so-called “region-growing propagation mechanism”). Rooting is performed during the *TdA2* behavior. This behavior is launched for each tissue only if a valid model has been locally estimated for the considered tissue. At each execution of this behavior, a candidate voxel is chosen from the center of the labeling territory to its periphery and evaluated. The seed selection criterion is more selective than the criteria used during the region-growing process. It is computed by evaluating the gray level of voxels situated inside a small region centered upon the voxel concerned (with radius R_r , typically equal to 2). If the ratios of voxels in this area that verify, respectively, the sufficient radiometric criteria (1) and the necessary radiometric criteria (2) are higher than predefined thresholds (respectively, 0.6 and 0.8), the voxel is selected as the seed. The *TdA3* behavior is then triggered and the region-growing process starts from the seed. If no voxel can be selected after a given number of executions of the rooting behavior *TdA1*, or when a region-growing process in a neighboring partition reaches the boundary of the partition concerned before the selection of a seed, the rooting behavior *TdA2* stops. The region-growing behavior *TdA3* is then selected and triggered, from the candidate voxels given by the neighboring agent, as soon as they are available.

Region growing. Starting from a seed, the region-growing process is performed by assessing every voxel situated at the current region boundary in 18-connexity. This is

performed by the behavior *TdA3*. Two steps are executed alternatively. In a first step, region growing is performed using the sufficient radiometric criterion (1) until a given number of voxels has been aggregated or until no more voxels can be aggregated. In a second step, the remaining candidate-voxel list is re-evaluated using the necessary radiometric criterion (2) and the topologic criterion (3). Voxels are aggregated if they fulfill both criteria. If the growing region reaches the boundary of a neighboring territory, candidate voxels are stored in the candidate list of the corresponding agent. When no more voxels can be aggregated, the agent is deactivated until new candidate voxels are provided by a neighboring agent. In this case the agent is automatically reactivated to process them. When all tissue-dedicated agents detect that a given ratio of voxels in their perception territory (typically 0.9) have been labeled (i.e. when a large enough under-segmentation is locally available to refine the model estimation), the *TdA3* behaviors of all tissue-dedicated agents are stopped automatically and the *LcA3* behavior (final radiometric model estimation) is launched. Otherwise, the behavior change is triggered by a group coordination mechanism when the largest possible under-segmentation is obtained in every remaining partition (i.e. when all remaining agents of the initial labeling group have terminated the initial phase and become inactive).

2.2.5.2. Final phase (competitive labeling). Voxels unlabeled during the initial phase (usually voxels lying at the edge between tissues) are treated during the final phase. The labeling is performed by the *LcA4* behavior when the final models have been checked by all tissue-dedicated agents. Voxel classification is done competitively between tissues, from the most reliable labeling to the most uncertain one. For each tissue type t , every candidate voxel v is evaluated using the following evaluation function: $E(v) = \beta \times G(I(v), \theta_t) + (1 - \beta) \times L(v, t)$, where G is the Gaussian model whose parameters θ_t have been set during the behavior *TdA3*. β allows for weighting the importance of the radiometric and compactness criteria (typically it is equal to 0.8). The candidate voxel with the higher evaluation for each tissue is then given to the local control agent. The latter ultimately decides to label the candidate voxel provided by the tissue-dedicated agent, which has the higher evaluation.

New agents dedicated to tissue mixtures (WM-GM and CSF-GM) can be introduced at the beginning of the final labeling step with a corresponding evaluation criterion. New labels are then introduced into the decision maps for voxels containing mixtures of tissue.

3. Evaluation

The evaluation was performed using two complementary approaches. A quantitative approach which meant comparing our method with representative methods in the literature based on realistic MRI phantoms. A qualitative evaluation was also performed on real MRI brain scans to illustrate some of the main features of our approach. In both cases a skull-stripping map [27] was computed and applied firstly to differentiate brain tissue from the remainder of the image.

Phantom images were generated using the BrainWeb simulator [8]. Starting with images where tissue classification was known, we created volume images with several noise levels

(3, 5, 7 and 9%), and non-uniformity of intensity (0, 20 and 40%). We compared our results with three well-known MRF-based methods including shading effect correction: SPM [2], FSL [33] and EMS [31] (results from other methods are available in [25]). For each tissue, we calculated the true positive (TP), the false positive (FP), the true negative (TN) and the false negative (FN) voxel classification rate, and then the Jaccard coefficient (as equal to $TP/(TP + FP + FN)$). Twelve images with matrix size = $181 \times 217 \times 181$ and voxel size = 1 mm^3 were used for quantitative evaluation.

Global histograms, computed on the simulated images as well as tissue histograms, computed from the reference image, are shown in Fig. 5. As can be seen, the higher the noise, the higher the overlapping between tissue; the higher the non-uniformity of intensity, the higher the standard deviation for each tissue. Note that a noise level equal to zero is unrealistic but shows more specifically how tissue-intensity distributions are hampered by the effects of non-uniformity and partial volume. In fact, no pure Dirac intensity distributions were observed on the 0% noise, 0% non-uniformity histogram.

Three dimensional anatomical brain scans (T1-weighted, 3D flash sequence, voxel size = 1 mm^3 , matrix size = $181 \times 184 \times 157$) were acquired at 1.5 T on a clinical MR scanner (Philips ACS II) for the purpose of qualitative evaluation. Such images are shown in Figs. 7a and 8a. Fig. 7 shows the high variability of tissue characteristics depending on the position in the real image.

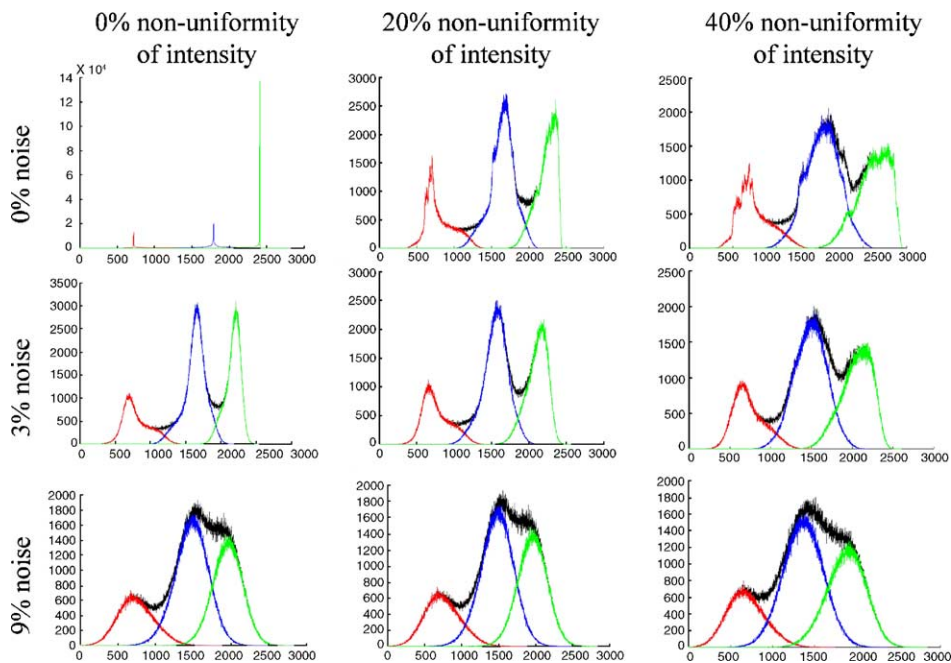


Fig. 5. Global histograms on a set of simulated images. Nine simulated images, generated with BrainWeb Simulator [8], are shown with three values, 0, 20 and 40%, of non-uniformity of intensity and three values, 0, 3 and 9%, of noise. Thick black curves correspond to raw data. Fine curves correspond to tissue histograms computed using the reference image.

4. Results

4.1. Quantitative evaluation

For phantom-image segmentation, the anatomical volume was partitioned using a $30 \times 30 \times 30$ voxel-size grid. Four agents were considered per cube, namely one local control agent and three tissue-dedicated agents, i.e. three agents dedicated to pure tissue (WM, GM and CSF) segmentation. In all, 138 local control agents and 414 tissue-dedicated agents were launched achieving the image volume segmentation in 2 min on a PC486, 256M RAM, 800 MHz. $30 \times 30 \times 30$ voxel size perception and labeling territories were assigned to each local control agent. Successive decision maps sequentially extracted during the segmentation process are shown in Fig. 6 for a phantom image (3% noise, 20% intensity non-uniformity).

The results of the evaluation are shown in Table 1. Three levels of non-uniformity for the four levels of noise were considered. The Jaccard coefficient was calculated for each method and for each tissue.

4.2. Qualitative evaluation

For real MRI brain scan segmentation, the anatomical volume was partitioned following a $15 \times 15 \times 15$ voxel size grid. Six agents were considered per cube: one local control agent and five tissue-dedicated agents, i.e. three agents dedicated to pure tissue (WM, GM and CSF) segmentation and two agents dedicated to mixed-tissue segmentation (WM-GM and CSF-GM). Overall, 686 local control agents and 3430 tissue-dedicated agents were launched, achieving segmentation in 5 min on a PC486, 256M RAM, 800 MHz.

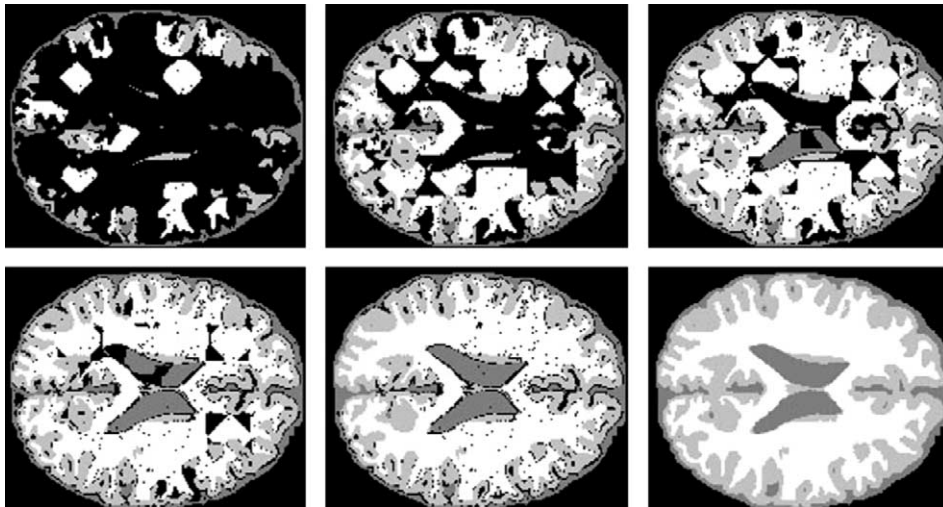


Fig. 6. Successive decision maps gradually produced by the system for a simulated image (3% noise, 20% non-uniformity of intensity). As can be seen, a progressively more complete labeling of the image volume is achieved.

Table 1

Results on Brainweb phantom images [8] for three well-known methods and the approach we propose

	<i>n</i> = 3%			<i>n</i> = 5%			<i>n</i> = 7%			<i>n</i> = 9%		
	0%	20%	40%	0%	20%	40%	0%	20%	40%	0%	20%	40%
SPM [2]												
WM	0.89	0.89	0.88	0.86	0.87	0.87	0.81	0.81	0.82	0.75	0.76	0.76
GM	0.77	0.78	0.79	0.74	0.75	0.76	0.68	0.70	0.71	0.63	0.64	0.66
CSF	0.47	0.49	0.50	0.47	0.48	0.50	0.45	0.47	0.48	0.41	0.43	0.45
EMS [31]												
WM	0.85	0.84	0.85	0.83	0.83	0.83	0.79	0.79	0.72	0.73	0.73	0.73
GM	0.80	0.79	0.81	0.79	0.79	0.80	0.75	0.76	0.70	0.71	0.71	0.72
CSF	0.59	0.60	0.60	0.60	0.60	0.60	0.56	0.57	0.56	0.53	0.53	0.53
FSL [33]												
WM	0.91	0.93	0.88	0.91	0.89	0.88	0.88	0.88	0.88	0.86	0.86	0.86
GM	0.85	0.86	0.84	0.85	0.84	0.84	0.83	0.84	0.83	0.82	0.82	0.82
CSF	0.56	0.57	0.58	0.54	0.55	0.55	0.53	0.54	0.55	0.53	0.54	0.54
Our approach												
WM	0.88	0.88	0.87	0.87	0.87	0.86	0.86	0.86	0.85	0.83	0.83	0.82
GM	0.84	0.83	0.83	0.84	0.84	0.83	0.83	0.83	0.83	0.80	0.80	0.79
CSF	0.58	0.58	0.59	0.58	0.59	0.59	0.57	0.58	0.58	0.54	0.55	0.55

For each level of noise, three levels of non-uniformity of intensity are considered. The computation of Jaccard coefficient, $(TP/(TP + FP + FN))$ is reported for the three tissues WM (white matter), GM (gray matter) and CSF (cerebrospinal fluid) and for the voxels outside the brain (“Other” class). TP: true positive, FP: false positive, FN: false negative.

$20 \times 20 \times 20$ voxel size perception and $15 \times 15 \times 15$ voxel size labeling territories were assigned to each local control agent.

Fig. 7 illustrates the importance of local model adaptation on two different cubes (B8 and F2 in Fig. 7a). The corresponding local histograms are shown in (Fig. 7c). As indicated in Fig. 7c, the GM intensity distribution of the upper cube appears equal to the WM intensity distribution of the lower cube. However, thanks to local adaptation, the global result is satisfactory, as indicated in Fig. 7b.

Another experiment was conducted to emphasize some potential difficulties of the partitioning strategies. Two cases are illustrated in Fig. 8:

- Case 1: the presence of different anatomical structures composed of the same tissue, but with different intensity distribution, hampers the model estimation;
- Case 2: due to the reduced size of the voxel population, the model estimation fails for some tissue.

Cooperation between neighboring agents and interpretation refinement are the solutions we offer to cope with these difficulties, as illustrated in Fig. 8. Fig. 8a shows a partial view of a brain section where several tissues distributed over different anatomical structures appear. The GM tissue is observed inside two different structures, the cortex on the one hand and the central structures (mainly the putamen) on the other, where intensity distribution is intermediate between the intensity distributions of the WM and the cortical GM. These tissues are not uniformly represented in each cube of our grid. In C-3, the

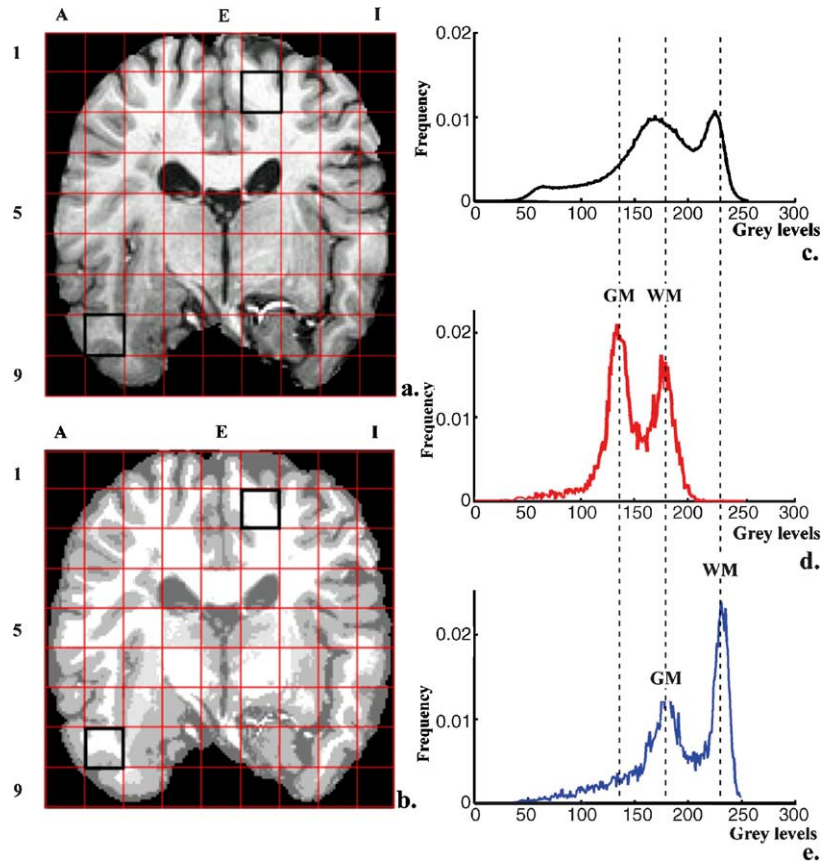


Fig. 7. A segmentation example. (a) The partitioning grid is placed on one real MR anatomical slice. (b) The final segmentation. Based on local Gaussian estimates, the final segmentation is correctly performed especially in zones difficult to segment such as B-8. (c) The global histogram over the entire volume is plotted. (d,e) Local histograms corresponding to two cubes located at B-8 (d) and F-2 (e). Note that gray matter peak in F-2 corresponds to white matter in B-8.

putamen is present whilst in D-4, WM is largely present. C-3 and D-4 are illustrative of Case 1 and Case 2, respectively. Progressive estimation of the corresponding Gaussian models is illustrated in Fig. 8d–g, where d–g, respectively, correspond to the initial and final phases of segmentation.

4.3. Initial model estimation

Fig. 8d shows the result of initial model estimation. Some models are missing in D-4, due to the absence of some tissue and also in C-3, due to the presence of a supplementary intensity distribution, corresponding to the putamen, between the distribution of cortical GM and WM. In C-3, this led to a misinterpretation: the putamen peak is interpreted as a GM peak and the cortical GM peak is interpreted as a CSF peak.

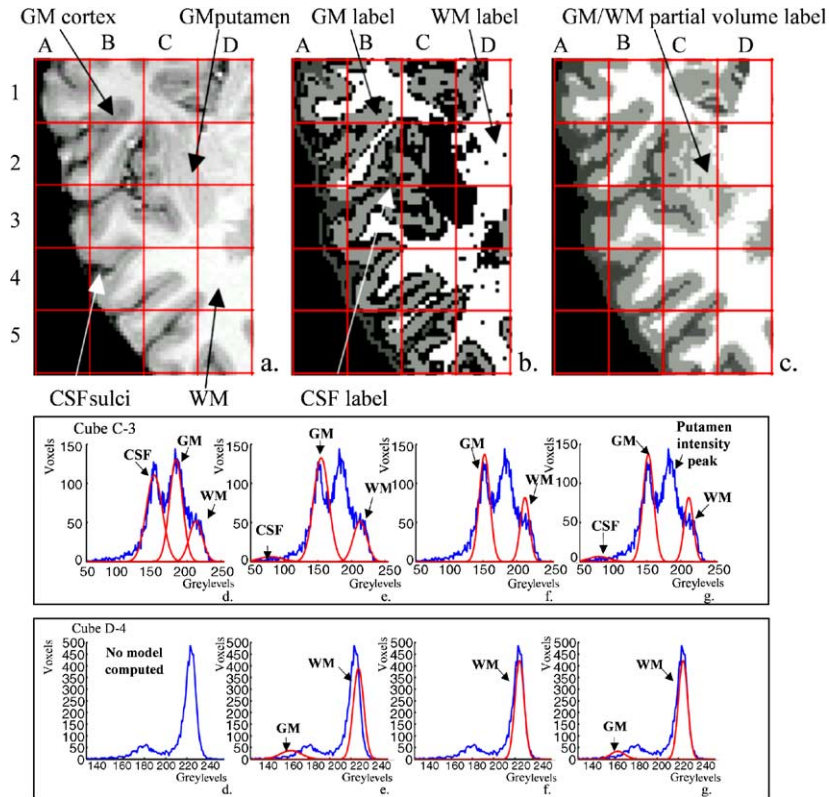


Fig. 8. Refinement of the model estimation. (a) A selected zone excerpt from a real MR anatomical image and the corresponding partitioning grid. Two cubes are selected: C-3 which contains putamen and D-4 where essentially white matter is present. (b) Under-segmented image obtained at the end of the initial phase. (c) Final segmentation image. (d–g) Progressive interpretation for cube C-3 and D-4. Local histograms and estimated Gaussian models are shown at four interpretation steps starting with d: initial Gaussian estimation, and ending with g: model checking in the final phase.

4.4. Initial model checking

During the successive interpretation steps (Fig. 8e), these Gaussian models are checked, corrected and/or computed by interpolation from the neighboring models. False models were corrected in C3 based on the neighborhood. The putamen is a small structure not present in a majority of neighbors. Thus, the GM model computed corresponded to cortical GM. Missing models in D-4 were also computed.

4.5. Initial labeling

These models were used during the initial phase to compute an under-segmented image, shown in Fig. 8b. Note that at this step, the putamen stayed mostly unlabeled because its intensity was intermediate between the cortical GM and WM models.

4.6. Final model estimation

During the final phase, this under-segmentation was used to re-estimate the Gaussian models (Fig. 8f). Some models were refined in this way, for instance the WM model in D-4, and the GM model in C-3.

4.7. Final model checking

Once again, the resulting models were then checked, missing ones were computed, for instance the CSF model in C-3, and the GM model in D-4.

4.8. Final labeling

They were used to label the remaining voxels in the final segmentation, shown in Fig. 8c. Additional labels corresponding to WM-GM and CSF-GM partial volume effect were added in the final labeling phase. Most of the voxels belonging to the putamen structure were labeled as WM-GM partial volume voxels.

5. Discussion and conclusion

In this paper, we propose a framework based on situated and cooperative agents for the management of the various information processing steps required for the localization of cerebral tissue in MRI brain scans. Our approach relies on: (1) the introduction of spatially distributed model estimation and classification to deal with *spatially non-uniform intensity* issues, (2) the introduction of a model refinement and a coarse to fine labeling strategy based on fusion mechanisms to deal with the issue of *noise and partial volume*, and (3) the use of a *multi-agent architecture* to design an opportunist system where information is extracted incrementally, the most robust being extracted first and propagated via information sharing and coordination mechanisms, to gradually construct final decision making.

5.1. Adaptation to intensity non-uniformity

Several models have been proposed in the literature to take into account *spatially non-uniform intensity*. A smooth and slowly varying multiplicative map, called a bias field map, is calculated based on bias field models [2,25,28,30]. Smooth spatial functions, or the Markov random field (MRF) model [15], can be used for this purpose. Spatially variant intensity distribution models may also be introduced using similar smooth functions [20,22]. Three main model instantiation strategies are then proposed. The first strategy consists in the estimation of a bias field map during a preprocessing step. No tissue models are introduced. The estimation is performed by homomorphic filtering [6] or optimization of a quality criterion of the image intensity distribution (frequency content maximization [26] or entropy minimization [18]). The second strategy consists in iterating voxel classification and model estimation (bias field model and spatially varying tissue intensity models) in optimal global approaches. In the context of EM probabilistic classification, in

the three methods reported in Table 1, EMS, SPM and FSL, the bias field model is estimated from the computation of posterior tissue probability maps. The bias estimation is obtained by fitting a polynomial function [30], a cosinus function [2] similar to [32], and by low pass filtering of the residual bias [33] used to correct the gray level map before the estimation of tissue-intensity models. Similar approaches have been also proposed in the context of fuzzy classification [1,21]. The third strategy consists in estimating locally (on small volumes) spatially distributed tissue-intensity models. These local models are then used to compute spatially variant intensity models by interpolation of the estimated models at each voxel location [12,22], or to compute a multiplicative bias field map [25] used to correct, image gray levels during a preprocessing step.

Our approach follows this latter strategy to instantiate spatially variant tissue intensity models. As in [12,16], we fitted density functions to the local histograms of the image. The models estimated in “perception territories” are used to label voxels in “labeling territories”, whose size is equal to, or smaller than, the “perception territories”. To speed up the segmentation, inside “labeling territories” we neglected non-uniformity of intensity and considered the intensity model parameters as constant. The choice of the size of perception territories is a tradeoff: in very small territories the validity of the distribution model estimation is not guaranteed (three types of tissue are not present in most territories), whilst in very large territories, non-uniformity of intensity cannot be considered valid. Empirically, we have fixed the mean size of each cube at 20 voxels (between 15 for some real images and 50 for some phantom images). A brain volume is then partitioned into approximately 150 cubes.

This local approach requires the use of mechanisms to manage situations where no local models can be estimated [12,25,34]. This is confirmed by the results shown in Fig. 8. We propose to control the validity of local models by (1) confronting them with models obtained in their neighborhood, (2) refining them during successive estimation steps. We use an overlapping grid to reinforce the coherence between adjacent models.

Local estimation of spatially distributed intensity models makes the performance of our system interesting. As reported by results shown in Fig. 8 on real MRI brain scans, this allows for correct estimation of tissue-intensity distribution in different locations in the image, despite large intensity variations inside the same tissue. When considering the four methods presented in Table 1, for a given noise level, the performances are maintained in spite of increasing non-uniformity of intensity. Calculation of an explicit bias field correction is a computational burden. Our distributed local modeling seems an interesting alternative to the costly computation of an explicit bias field model, especially when time is a critical issue.

5.2. Adaptation to noise and partial volume effect

To cope with the presence of noise in the images and maintain global coherence, interactions between neighboring voxel labels are often modeled. MRF models are introduced for this purpose in a Bayesian framework to define a priori tissue probabilities relative to the neighborhood. Two main strategies for model instantiation and voxel labeling are then commonly used. According to the first strategy [23], intensity model parameters are estimated from a gray level distribution fitting. Maximum a posteriori (MAP) voxel labeling is then computed using algorithms, such as iterative conditional

mode (ICM), or simulated annealing (SA). Here, MRF model parameters are a priori given. A second strategy consists in refining model estimation iteratively during the interpretation process. This is elegantly performed in the context of probabilistic Bayesian classification via the EM algorithm. In the estimation step, the a posteriori probability that voxels belong to tissue are computed by fusing probabilities provided by the current intensity and MRF models. During the maximization step, the previously obtained probabilities are then used to refine intensity and MRF models. In Table 1, two methods, EMS and FSL, use MRF model with the second strategy. In FSL, the MRF model is applied to tissue label maps, and not to posterior probability maps, as with EMS. In EMS, MRF parameters are iteratively optimized when they are set in FSL. SPM, FSL and EMS perform an iterative refinement of intensity model parameters. These distinctions can explain the differences in the two methods reported in Table 1.

Instead of MRF modeling, we introduced voxel interactions via the fusion of a topological criterion and radiometric criteria. Voxels are not labeled in an optimal way but incrementally in two phases, from the most reliable to the most uncertain. A fast region-growing process is used during the initial phase, and competitive labeling, based on an evaluation function, is used for the most difficult voxels during the final phase. Similarly, tissue-intensity models are refined during the two phases. Contrary to global approaches, such as in [2,31,33], and similarly to approaches based on local estimation on spatially distributed intensity models [12,25,34], the partial volume effect is taken into account in our approach. An explicit Gaussian curve is introduced to model intensity distribution of voxels containing tissue mixtures. Specific partial volume labels can also be introduced using our approach, depending on the application.

The evaluation on MNI phantom images shows, for all methods including ours, that the higher the noise, the lower the accuracy of segmentation. CSF and GM appears more difficult to segment compared to WM for all methods, which is mainly due to partial volume effect. However, we obtain better results than two of the tested methods SPM [2] and EMS [31]. Note that the loss of accuracy when noise increases is above 10% for the two first methods (SPM and EMS), and around 5% for FSL [33] and our own method. FSL obtains better results in comparison with our method. However, because it follows an optimal strategy (MRF approach), and estimates a bias field model, the computational cost of this method appears higher compared to ours: less than 5 min to segment a $181 \times 217 \times 181$ complete volume for our system, and 20 min for FSL and EMS. FSL and our method both use the same algorithm for automated brain extraction [27]. The same values for Jaccard coefficients are then obtained for labeling voxels outside the brain (see “other class” in Table 1) for these two methods. EMS and SPM use an atlas for brain extraction and for insertion of a priori probability for Bayesian classification. As indicated in Table 1, voxels outside the brain seem better segmented with automated extraction algorithms [27] than with atlas-based matching methods.

5.3. The multi-agent architecture

Multi-Agent architectures have already been proposed for low level feature extraction [9,11,19] or knowledge-based scene interpretation [5,10]. In [19], reactive agents are designed to label homogeneous fine structures. Agents are provided with different

behaviors such as perception, to assess from local characteristics whether a voxel belongs to a segment, labeling, breeding or diffusion. Breeding and diffusion are achieved in preferential directions that are learned from the success of previous displacements of agents. Duchesnay et al. [9] propose an agent society organized as an irregular pyramid where region and edge agents collaborate.

Our approach is close to those proposed in [5] for the segmentation and analysis of a sequence of moving cell images and in [10] for automatic target recognition. Situated agents are introduced, which are specialized and use the prior knowledge function of the objects present in the image to be interpreted, depending on their location in the image, and depending on the treatment they have to achieve to reach their goals. Each agent works locally, shares results via a common information zone and specific maps, and coordinates its actions with other agents to reach a common global goal. When available, extracted information, such as model parameters or voxel candidates for region aggregation, is provided to relevant agents. The use of sophisticated agent communication language is not required and would greatly hamper the efficiency of the system. The parallel execution of distributed treatments is currently simulated. The framework could easily be adapted to a parallel hardware environment to speed up the interpretation process.

Based on our experiments with phantom images and real MRI brain scans, situated and cooperative agents appear as an interesting framework to implement treatment required for tissue interpretation. As shown with the case of the putamen, structure identification should be performed to improve tissue identification. For this purpose, anatomical knowledge should be introduced using, for instance, possibilistic logic [3]. This can be elegantly performed into our framework via the insertion of new maps, new models and new agents to manage them.

Acknowledgements

Nathalie Richard has a Ph.D. grant from the Centre National de la Recherche Scientifique (CNRS).

References

- [1] Ahmed M, Yamany S, Mohamed N, Farag A, Moriarty T. A modified fuzzy c-means algorithm for bias field estimation and segmentation of MRI Data. *IEEE Trans Med Imag* 2002;21:193–9.
- [2] Ashburner J, Friston K. Multimodal image coregistration and partitioning—a unified framework. *NeuroImage* 1997;6:209–17.
- [3] Barra V, Boire JY. Automatic segmentation of subcortical brain structures in MR images using information fusion. *IEEE Trans Med Imag* 2001;20:549–58.
- [4] Bloch I. Information combination operators for data fusion: A comparative review with classification. *IEEE Trans Syst, Man, Cyb* 1996;26:52–67.
- [5] Boucher A, Doisy A, Ronot X, Garbay C. A society of goal-oriented agents for the analysis of living cells. *Artif Intel Med* 1998;14:183–99.
- [6] Brinkmann BH, Manduca A, Robb RA. Optimized homomorphic unsharp masking for MR grayscale inhomogeneity correction. *IEEE Trans Med Imag* 1998;17:161–71.
- [7] Clancey C. *Situated Cognition*. Cambridge University Press, 1997.

- [8] Collins D, Zijdenbos A, Kollokian V, Sled J, Kabani N, Holmes C, et al. Design and construction of a realistic digital brain phantom. *IEEE Trans Med Imag* 1998;17:463–8.
- [9] Duchesnay E, Montois J-J, Jacquelet Y. Cooperative agents society organized as an irregular pyramid: A mammography segmentation application. *Pattern Recognit Lett* 2003;24:2435–45.
- [10] Ealet F, Collin B, Sella G and Garbay C. A multi-agent architecture for scene interpretation. In: J. Verly, editor. *AEROSENSE'2000*, SPIE Proc 2000;4023:236–47.
- [11] Germond L, Dojat M, Taylor C, Garbay C. A cooperative framework for segmentation of MRI brain scans. *Artif Intell Med* 2000;20:77–94.
- [12] Grabowski TJ, Frank RJ, Szumski NR, Brown CK, Damasio H. Validation of partial tissue segmentation of single-channel magnetic resonance images of the brain. *NeuroImage* 2000;12:640–56.
- [13] Gutknecht O, Michel F, Ferber J. Integrating tools and infrastructures for generic multi-agents systems. Montreal, Canada: ACM, 2001.
- [14] Hata Y, Kobashi S, Hirano S, Kitagaki H, Mori E. Automated segmentation of human brain MR images aided by fuzzy information granulation and fuzzy inference. *IEEE Trans Syst, Man, Cybernet* 2000;30:381–95.
- [15] Held K, Kopps ER, Krause BJ, Wells WM, Kikinis R, Muller-Gartner HW. Markov random field segmentation of brain MR images. *IEEE Trans Med Imag* 1997;16:878–86.
- [16] Joshi M, Cui J, Doolittle K, Joshi S, Van Essen D, Wang L, et al. Brain segmentation and the generation of cortical surfaces. *NeuroImage* 1999;9:461–76.
- [17] Laidlaw DH, Fleischer KW, Barr AH. Partial-volume bayesian classification of material mixtures in MR volume data using voxel histograms. *IEEE Trans Med Imag* 1998;17:74–86.
- [18] Likar B, Viergever MA, Pernus F. Retrospective correction of MR intensity inhomogeneity by information minimization. *IEEE Trans Med Imag* 2001;20:1398–410.
- [19] Liu J, Tang YY. Adaptive image segmentation with distributed behavior-based agents. *IEEE Trans Patt Anal Mach Intell* 1999;21:544–51.
- [20] Marroquin JL, Vemuri BC, Botello S, Calderon F, Fernandez-Bouzas A. An accurate and efficient bayesian method for automatic segmentation of brain MRI. *IEEE Trans Med Imag* 2002;21:934–45.
- [21] Pham D, Prince J. Adaptive fuzzy segmentation of magnetic resonance images. *IEEE Trans Med Imag* 1999;18:737–52.
- [22] Rajapakse J, Kruggel F. Segmentation of MR images with intensity inhomogeneities. *Im Vis Comput* 1998;16:165–80.
- [23] Ruan S, Jaggi C, Xue J, Fadili J, Bloyet D. Brain tissue classification of magnetic resonance images using partial volume modeling. *IEEE Trans Med Imag* 2000;19:1179–87.
- [24] Schroeter P, Vesin J-M, Langenberger T, Meuli R. Robust parameter estimation of intensity distributions for brain magnetic resonance images. *IEEE Trans Med Imag* 1998;17:172–86.
- [25] Shattuck DW, Sandor-Leahy SR, Schaper KA, Rottenberg DA, Leahy RM. Magnetic resonance image tissue classification using a partial volume model. *NeuroImage* 2001;13:856–76.
- [26] Sled JG, Zijdenbos AP, Evans A. A non-parametric method for automatic correction of nonuniformity in MRI data. *IEEE Trans Med Imag* 1998;17:87–97.
- [27] Smith S. Fast robust automated brain extraction. *Human Brain Mapp* 2002;17:143–55.
- [28] Styner M, Brechbühler C, Székely G, Gerig G. Parametric estimate of intensity inhomogeneities applied to MRI. *IEEE Trans Med Imag* 2000;19:153–65.
- [29] Teo PC, Sapiro G, Wandell BA. Creating connected representations of cortical gray matter for functional MRI visualization. *IEEE Trans Med Imag* 1997;16:852–63.
- [30] Van Leemput K, Maes F, Vandermeulen D, Suetens P. Automated model-based bias field correction in MR images of the brain. *IEEE Trans Med Imag* 1999;18:885–96.
- [31] Van Leemput K, Maes F, Vandermeulen D, Suetens P. Automated model-based tissue classification of MR images of the brain. *IEEE Trans Med Imag* 1999;18:897–908.
- [32] Wells WM, Grimson WEL, Kikinis R, Jolesz FA. Adaptive segmentation of MRI data. *IEEE Trans Med Imag* 1996;15:429–42.
- [33] Zhang Y, Brady M, Smith S. Segmentation of Brain MR images through a hidden Markov random field model and the expectation–maximisation algorithm. *IEEE Trans Med Imag* 2001;20:45–57.
- [34] Zhu C, Jiang T. Multicontextual fuzzy clustering for separation of brain tissues in magnetic resonance images. *NeuroImage* 2003;18:685–96.